Magnetic order and magnetoelectric properties of R_2CoMnO_6 perovskites (R = Ho, Tm, Yb, and Lu)

J. Blasco,[1,*] J. L. García-Muñoz,[2] J. García,[1] G. Subías,[1] J. Stankiewicz,[1] J. A. Rodríguez-Velamazán,[1,3] and C. Ritter[3]

[1]*Instituto de Ciencia de Materiales de Aragón, Departamento de Física de la Materia Condensada, Consejo Superior de Investigaciones Científicas (CSIC)–Universidad de Zaragoza, E-50009 Zaragoza, Spain*

[2]*Institut de Ciència de Materials de Barcelona (ICMAB)-CSIC, Campus de la Universitat Autònoma de Barcelona–Bellaterra, E-08193 Bellaterra, Spain*

[3]*ILL-Institut Laue Langevin, 71, Avenue des Martyrs, 38042 Grenoble Cedex, France*

(Received 21 April 2017; published 10 July 2017)

We present a detailed study on the magnetic structure and magnetoelectric properties of several double perovskites R_2CoMnO_6 (R = Ho, Tm, Yb, and Lu). All of these samples show an almost perfect ($\sim 94\%$) ordering of Co^{2+} and Mn^{4+} cations in the unit cell. Our research reveals that the magnetic ground state strongly depends on the R size. For samples with larger R (Ho and Tm), the ground state is formed by a ferromagnetic order (F type) of Co^{2+} and Mn^{4+} moments, while R either remains mainly disordered (Ho) or is coupled antiferromagnetically (Tm) to the Co/Mn sublattice. For samples with smaller R (Yb or Lu), competitive interactions lead to the formation of an E-type arrangement for the Co^{2+} and Mn^{4+} moments with a large amount of extended defects such as stacking faults. The Yb^{3+} is partly ordered at very low temperature. The latter samples undergo a metamagnetic transition from the E into the F type, which is coupled to a negative magnetodielectric effect. Actually, the real part of dielectric permittivity shows an anomaly at the magnetic transition for the samples exhibiting an E-type order. This anomaly is absent in samples with F-type order, and, accordingly, it vanishes coupled to the metamagnetic transition for R = Yb or Lu samples. At room temperature, the huge values of the dielectric constant reveal the presence of Maxwell-Wagner depletion layers. Pyroelectric measurements reveal a high polarization at low temperature, but the onset of pyroelectric current is neither correlated to the kind of magnetic ordering nor to the magnetic transition. Our study identified the pyroelectric current as thermally stimulated depolarization current and electric-field polarization curves show a linear behavior at low temperature. Therefore, no clear ferroelectric transition occurs in these compounds.

DOI: 10.1103/PhysRevB.96.024409

I. INTRODUCTION

The revival in the study of multiferroic compounds in recent years has stimulated the search for new materials with significant magnetoelectric coupling in a wide temperature range [1–4]. Strong magnetoelectric coupling is expected for systems where the ferroelectricity is induced directly by the spin order. However, the symmetry restrictions for possible magnetic orders that can induce ferroelectricity lead to noncollinear structures that are normally found in frustrated systems with low transition temperatures [5–7]. Nevertheless, there is a promising exception to this trend: the collinear E phase characterized by up-up-down-down ($\uparrow\uparrow\downarrow\downarrow$) spin chains along a particular crystallographic direction [8–10]. This magnetic ordering along with electric polarization (P) was first observed [8] in orthorhombic $HoMnO_3$. Monte Carlo calculations predicted that the symmetry of these spin chains coupled to the buckling distortions of oxygen octahedra leads to the formation of a polar axis perpendicular to the magnetic order direction [9]. As competing magnetic interactions—ferromagnetic (FM) nearest neighbor (NN) and antiferromagnetic (AFM) next-nearest neighbor (NNN) exchanges—are important to form an E-type order, perovskites with small rare earth atoms are good candidates for it [8,10].

Subsequent first principle calculations suggested that this mechanism could also be operative in double perovskites with $A_2BB'O_6$ nominal formula [11], i.e., a perovskite compound with cationic ordering at the B site. It could be an important step forward since strong B-O-B' superexchange interactions may lead to ordering temperatures (T_N) above liquid nitrogen temperature. The theoretical calculations performed on a nominal Y_2NiMnO_6 yield a polar ground state with $P = 2.5\,\mu C/cm^2$. Later, the first double perovskite with E phase was found in Lu_2CoMnO_6 with $T_N \sim 50$ K and a magnetic anomaly in the dielectric permittivity at the same temperature. The magnetic ordering is established along the c axis, and pyroelectric measurements on a polycrystalline sample [12] revealed a small $P \sim 2\,\mu C/m^2$ that disappears when applying a magnetic field (negative magnetocapacitance). However, a study on a single crystal [13] showed an anisotropic behavior of the dielectric permittivity, and the anomaly appears only when the electric field is parallel to the b axis, in agreement with first principle calculations [9,11] and symmetry analysis [14]. Nevertheless, no ferroelectric transition is observed at T_N. Our previous study on Yb_2CoMnO_6 also confirmed the occurrence of an E-type ordering along the c axis for this compound [15]. Negative magnetocapacitance is also observed, and it is correlated with a metamagnetic transition. An external magnetic field destabilizes the E phase and favors a collinear FM ordering of Co^{2+} and Mn^{4+} magnetic

*Present address: Instituto de Ciencia de Materiales de Aragón, CSIC-Universidad de Zaragoza, Pedro Cerbuna 12, 50009 Zaragoza, Spain. Corresponding author: jbc@unizar.es

moments (F phase) that is coupled to the disappearance of the dielectric anomaly [15]. In agreement with the study on the Lu_2CoMnO_6 single crystal [13], we did not find ferroelectric transition at T_N in our Yb_2CoMnO_6 ceramic specimen.

G. Sharma *et al.* reported that Y_2CoMnO_6 undergoes a ferroelectric transition at 80 K driven by an E-type magnetic ordering [16]. The main evidence put forward was the existence of a reversible pyroelectric current with an onset of the corresponding electrical polarization at temperatures close to $T_N \sim 80$ K. In addition, a partial suppression of the electric polarization, observed after applying a magnetic field of 5 T, suggests a significant magnetoelectric coupling. This report is supported by first principle calculations that yield a magnetic ground state of an E-type order in competition with F- and A-type orderings [17].

However, our recent neutron diffraction study reveals that Y_2CoMnO_6 undergoes a FM transition. No ferroelectric transition is observed, but a pyroelectric effect arises from thermally stimulated depolarization currents [18]. We have found similar results in the study of the magnetoelectric properties of Er_2CoMnO_6 [19]. These results show the need of a thorough experimental characterization to determine the actual magnetic ground state of double perovskites with small A atoms and its relationship with the ferroelectric or magnetoelectric properties. The existence of metamagnetic transitions also reveals the strong competition between F- and E-type orders in this family of double perovskites and how small changes in the external conditions (magnetic field in this case) can modify the ground state properties in these systems.

In this paper, we report results of a comprehensive study on R_2CoMnO_6 (R = Ho, Tm, Yb, and Lu) double perovskites, which has been performed with two aims. First, we want to study the influence of the rare earth size on the magnetic ground state of these compounds in order to determine the stability range for E-type phases. Second, we intend to determine whether an E-type ordering is sufficient to develop ferroelectric ordering in these double perovskites.

II. EXPERIMENTAL SECTION

R_2CoMnO_6 compounds (R_2 = Ho_2, Tm_2, Yb_2, YbLu, and Lu_2) were prepared by ceramic procedures. Stoichiometric amounts of R_2O_3, Co_3O_4, and Mn_2O_3 with nominal purities not less than 99.9% were mixed, ground, and heated overnight at 900 °C. They were then ground again, pressed into pellets, and sintered at 1050 °C in air for 1 day. The pellets were reground, repressed, and sintered at 1250 °C for 2 days, followed by very slow cooling (0.2 °C/ min) down to 300 °C before the samples were extracted from the furnace. The last step is crucial to improve the cationic ordering at the perovskite B site and the oxygen stoichiometry [20,21]. The chemical composition of the samples was tested by using the wavelength dispersive x-ray fluorescence spectrometry technique. The cationic composition agreed with the nominal one for all samples within experimental errors.

Standard x-ray diffraction patterns were collected at room temperature using a Rigaku D/Max-B instrument with a copper rotating anode and a graphite monochromator to select the CuK_α wavelength. The device was working at 40 kV and 100 mA, and the measurements were performed in step-scanned mode from $18^\circ \leqslant 2\theta \leqslant 135^\circ$ in steps of 0.03°, with a counting rate of 6 s/step.

Neutron diffraction experiments were carried out at different temperatures at the high-flux reactor of the Institut Laue-Langevin (ILL), using two instruments. The high intensity diffractometer D1B was used to collect thermodiffractograms from 2 K up to temperatures well above the magnetic ordering. The device was working with a wavelength of 2.52 Å covering a useful angular range $5^\circ \leqslant 2\theta \leqslant 128^\circ$. On this instrument, measurements under a magnetic field were also performed for R = Yb and Lu. Sintered cylinders of the same composition were prepared, and a cryomagnet with a maximum field of $\mu_0 H = 5$ T was used. The magnetic field direction was oriented along the cylinder axis. The high resolution powder diffractometer D2B ($\lambda = 1.594$ Å) was used to perform crystallographic studies at selected temperatures. Structural refinements were made of both x-ray and neutron diffractograms by using the FullProf program [22]. The crystallographic tools from the Bilbao Crystallographic server [23–25] were also used.

Magnetic measurements were carried out between 2 and 300 K by using commercial Quantum Design (superconducting quantum interference device [SQUID] and Physical Property Measurement System [PPMS]) magnetometers. The dielectric measurements were carried out as a function of temperature between 5 and 300 K in a He cryostat employing a homemade coaxial-line inset. Sintered discs with diameter of ∼8 mm and thickness of ∼0.9 mm were used. Silver paint was applied to the disc surface for proper electrical contact. The complex dielectric permittivity of the samples was measured using an impedance analyzer (Wayne Kerr Electronics 6500B), applying voltages with amplitude of 1 V and a frequency range between 10 Hz and 5 MHz. Polarization versus electric-field loops were recorded using a commercial polarization analyzer (aixACCT Systems Easy Check 300) for frequencies up to 250 Hz and electric-field amplitude up to ∼20 kV/cm.

Pyroelectric current was measured with a Keithley 2635B electrometer by warming the sample at a constant rate with values ranging between 0.5 and 10 K/min. The change in the electrical polarization was obtained by integrating the pyroelectric current as a function of time. Different poling fields were tested. The electric field was applied at 150 K followed by cooling at a rate of 10 K/m down to 5 K. Then, the field was removed, and the stabilization of the polarization was reached after shorting the circuit for 15 m to remove surface charges.

III. RESULTS AND DISCUSSION

A. Crystal structure at room temperature

The x-ray patterns at room temperature established that all samples were single phase, exhibiting the monoclinic cell ($P2_1/n$ space group) typical of double perovskites. In order to determine the degree of Co/Mn ordering, high resolution neutron diffraction patterns were collected at 295 K. The refinements results are summarized in Table I. This technique confirms the high degree of Co/Mn ordering in the perovskite cell with an amount of antisite defects (ASDs), i.e., the number of Co and Mn atoms exchanging positions of typically ∼6% (50% implies random distribution). The five samples show

TABLE I. Refined structural parameters (lattice, fractional coordinates, temperature factors, bond lengths, and bond angles) and reliability factors from neutron patterns collected at 295 K for R_2CoMnO_6 (R_2 = Ho_2, Tm_2, Yb_2, YbLu, and Lu_2). The space group is $P2_1/n$ and the Wyckoff positions are indicated for each atom.

Sample	Ho_2CoMnO_6	Tm_2CoMnO_6	Yb_2CoMnO_6	$YbLuCoMnO_6$	Lu_2CoMnO_6
Lattice a (Å)	5.22487(6)	5.18998(6)	5.17698(4)	5.1692(1)	5.1603(1)
b (Å)	5.56795(6)	5.55221(6)	5.54841(4)	5.5474(1)	5.5421(1)
c (Å)	7.46649(8)	7.43221(8)	7.41821(6)	7.4153(1)	7.4127(1)
β (deg)	89.749(1)	89.713(1)	89.648(1)	89.632(1)	89.622(1)
Volume ($Å^3$)	217.212(4)	214.162(4)	213.076(3)	212.631(3)	211.992(4)
Coordinates					
R (4e): x	0.0180(2)	0.0204(3)	0.0215(1)	0.0208(2)	0.0207(3)
y	0.0713(2)	0.0740(2)	0.0750(1)	0.0749(1)	0.0749(3)
z	0.2509(3)	0.2515(3)	0.2513(1)	0.2516(2)	0.2513(2)
B ($Å^2$)	0.37(2)	0.35(2)	0.38(1)	0.16(1)	0.39(2)
Co (2d): (0 ½ 0)					
B ($Å^2$)	0.45(20)	1.24(16)	0.70(15)	0.60(16)	0.99(16)
Mn (2c): (½ 0 0)					
B($Å^2$)	0.75(12)	0.58(9)	0.42(8)	0.29(9)	0.26(9)
ASD (%)	6.3(5)	6.5 (8)	5.8(8)	6.4(9)	4.4(8)
O1 (4e): x	0.2989(4)	0.2995(4)	0.2998(3)	0.3006(3)	0.3009(4)
y	0.3164(5)	0.3169(4)	0.3190(4)	0.3194(4)	0.3189(4)
z	0.0510(3)	0.0532(2)	0.0547(2)	0.0549(2)	0.0554(3)
B ($Å^2$)	0.75(4)	0.48(3)	0.54(3)	0.27(3)	0.46(3)
O2 (4e): x	0.3178(4)	0.3219(3)	0.3248(4)	0.3250(3)	0.3246(4)
y	0.2938(4)	0.2937(4)	0.2945(4)	0.2961(3)	0.2963(4)
z	0.4441(3)	0.4412(3)	0.4402(3)	0.4397(2)	0.4391(3)
B ($Å^2$)	0.62(4)	0.54(4)	0.53(3)	0.37(3)	0.58(4)
O3 (4e): x	0.6053(3)	0.6116(3)	0.6138(3)	0.6151(3)	0.6164(3)
y	0.9655(3)	0.9617(3)	0.9582(3)	0.9573(3)	0.9570(3)
z	0.2563(3)	0.2570(3)	0.2573(3)	0.2570(2)	0.2571(3)
B ($Å^2$)	0.70(3)	0.55(3)	0.54(3)	0.33(3)	0.46(3)
Bond lengths					
Co-O1 (Å)	2.085(2)	2.081(2)	2.090(2)	2.089(2)	2.084(2)
Co-O2 (Å)	2.060(2)	2.070(2)	2.078(2)	2.072(2)	2.067(2)
Co-O3 (Å)	2.003(2)	2.010(2)	2.014(2)	2.014(1)	2.016(2)
$\langle Co-O\rangle_{av}$ (Å)	2.049(1)	2.054(1)	2.061(1)	2.058	2.056
Co-valence	+2.29(1)	+2.26(1)	+2.22(1)	+2.24	+2.25
Mn-O1 (Å)	1.906(2)	1.901(2)	1.895(2)	1.895(2)	1.896(2)
Mn-O2 (Å)	1.939(2)	1.926(2)	1.922(2)	1.929(2)	1.930(2)
Mn-O3 (Å)	1.908(2)	1.906(2)	1.905(2)	1.909(1)	1.909(2)
$\langle Mn-O\rangle_{av}$ (Å)	1.918(2)	1.911(2)	1.907(2)	1.911(2)	1.912(2)
Mn-valence	+3.85(1)	+3.92(1)	+3.96(1)	+3.92(1)	+3.91
Bond angles					
Co-O1-Mn (deg)	146.00(9)	145.22(9)	144.42(8)	144.18(8)	144.05(9)
Co-O2-Mn (deg)	145.35(9)	143.93(8)	143.10(9)	142.72(8)	142.57(9)
Co-O3-Mn (deg)	145.30(9)	143.23(9)	142.27(9)	141.86(6)	141.52(9)
$\langle Co-O-Mn\rangle_{av}$ (deg)	145.55(9)	144.13(8)	143.22(8)	142.93(6)	142.65(8)
R_B	3.18	3.09	3.33	3.52	3.82
R_{wp}	2.88	2.76	3.29	3.54	4.11
χ^2	1.93	1.81	2.64	2.81	1.55

the same crystal structure with similar lattice parameters and atomic positions. Clear trends are observed as the R size decreases (from R = Ho to R = Lu): (i) The unit cell volume decreases; (ii) The monoclinic distortion increases (β away from 90°); (iii) The Co-O-Mn bond angles decrease, indicating an increase of the tilting angle for $Co(Mn)O_6$ octahedra. In all compounds, the bond lengths agree with the presence of Co^{2+} and Mn^{4+} cations (see Table I). This result agrees with the findings using x-ray absorption near edge structure (XANES) spectroscopy in related double perovskites [21,26].

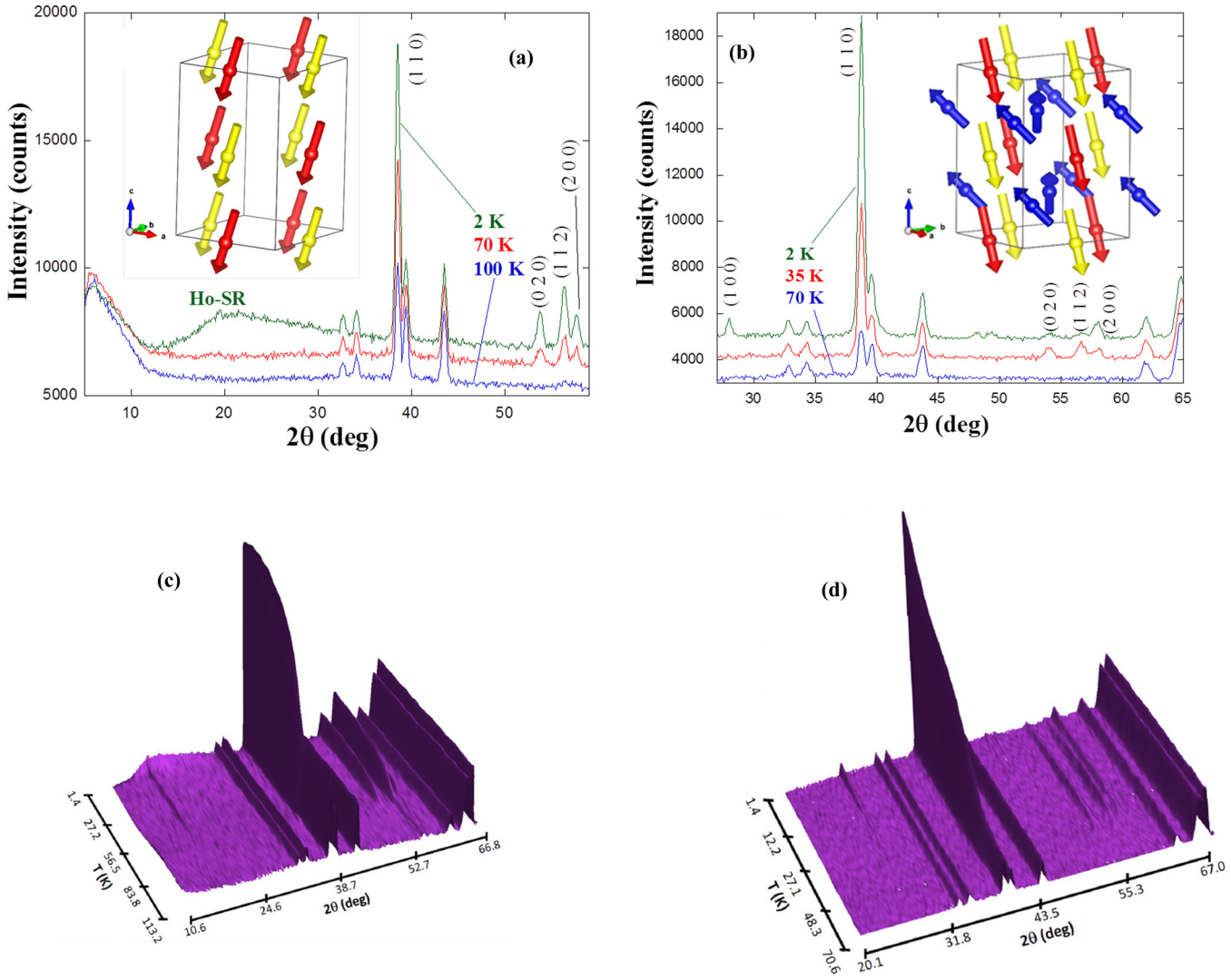

FIG. 1. Comparison of neutron patterns measured at selected temperatures for (a) Ho_2CoMnO_6 and (b) Tm_2CoMnO_6. Short-range contribution (Ho-SR) and some reflection indices are indicated in the (a) and (b) panels, respectively. Insets: Magnetic structure of the respective compounds. Yellow, red, and blue arrows stand for Mn, Co, and Tm moments, respectively. The temperature dependence of neutron diffractograms for (c) Ho_2CoMnO_6 and (d) Tm_2CoMnO_6.

B. Magnetic ordering in Ho_2CoMnO_6 and Tm_2CoMnO_6

The occurrence of long-range magnetic ordering was probed using neutron diffraction. Figure 1 compares neutron thermodiffractograms of Ho_2CoMnO_6 and Tm_2CoMnO_6. In the case of the latter sample, additional scattering ascribed to a long-range FM ordering is noticeable below ∼60 K. On further cooling, changes in the intensity of some peaks are detected below ∼30 K. Some of them experience a huge rise, such as (1 1 0), while others, i.e., (0 2 0), almost vanish. This points to a second magnetic transition or a magnetic reordering that is accompanied by a weak AFM component indicated by the appearing of (1 0 0) reflection.

Refinements of the neutron patterns below 59 K reveal a FM ordering of the Mn and Co moments. The strong structural distortion allows us to determine the moment direction, indicating that the spins are mainly oriented along the c axis. Therefore, the magnetic ordering follows the irreducible representation (Irrep) mGM_2^+, in agreement with related double perovskites [18,19,27]. This Irrep concurs with a magnetic arrangement of the $F_xA_yF_z$ type, following the Bertaut notation where $A_y = 0$ [28]. Therefore, the FM arrangement is established in the ac plane, and the refinement leads to the same moment for both atoms, which suggests that both Mn^{4+} and Co^{2+} are in high spin state with $S = 3/2$, as observed in related compounds [18,19,27,29]. Below 30 K, the changes in the magnetic scattering can be accounted for only by including the magnetic contribution from the Tm sublattice. Our refinements indicate that Tm^{3+} moments are antiferromagnetically coupled to the Mn-Co sublattice, in agreement with the usual negative J_{R-M} interaction found in perovskite compounds with heavy R (R = rare earth; $M = 3d$ transition metal) [19]. In order to have exact structural parameters, high resolution neutron patterns were collected at 2 and 25 K (see Supplemental Material [30]). The results are summarized in Table II. Our data reveal that at low temperature, the Co-Mn sublattice is highly polarized, achieving values of 2.85 μ_B/at, close to the

TABLE II. Refined structural parameters (lattice, fractional coordinates, temperature factors, and magnetic moments) and reliability factors from neutron patterns collected at low temperature for Tm_2CoMnO_6 and Ho_2CoMnO_6. The Wyckoff positions are indicated for each atom in $P2_1/n$ setting.

Sample	Tm_2CoMnO_6		Ho_2CoMnO_6
Temperature (K)	25	2	10
Lattice a (Å)	5.18906(9)	5.18943(9)	5.21923(8)
b (Å)	5.54327(9)	5.54304(10)	5.56359(8)
c (Å)	7.41875(13)	7.41935(14)	7.45218(11)
β (deg)	89.668(1)	89.674(1)	89.766(1)
Volume (Å^3)	213.392(6)	213.416(7)	216.392(6)
Coordinates R (4e): x	0.0199(4)	0.0208(4)	0.0194(3)
Y	0.0731(5)	0.0732(3)	0.0724(2)
Z	0.2522(4)	0.2520(4)	0.2509(3)
B (Å^2)	0.15(3)	0.04(3)	0.02(2)
Co (2d): B (Å^2)	0.22(18)	0.38(19)	0.06(17)
Mn (2c): B (Å^2)	0.48(11)	0.53(11)	0.10(11)
O1 (4e): x	0.3015(5)	0.3005(5)	0.2999(5)
y	0.3172(6)	0.3173(6)	0.3157(5)
z	0.0538(4)	0.0541(4)	0.0518(4)
B (Å^2)	0.21(5)	0.13(5)	0.15(5)
O2 (4e): x	0.3234(5)	0.3222(5)	0.3198(5)
Y	0.2933(6)	0.2934(6)	0.2923(5)
z	0.4420(4)	0.4423(4)	0.4451(4)
B (Å^2)	0.55(5)	0.46(5)	0.23(6)
O3 (4e): x	0.6119(4)	0.6123(4)	0.6047(4)
y	0.9611(4)	0.9626(4)	0.9667(4)
Z	0.2567(5)	0.2561(5)	0.2550(5)
B (Å^2)	0.46(5)	0.40(5)	0.19(4)
Mn-Co moment (μ_B/at): μ_x	1.02(13)	1.13(9)	0.84(10)
μ_z	−2.35(6)	−2.60(5)	−2.80(4)
μ_t	2.56(4)	2.83(6)	2.92(3)
Tm/Ho moment (μ_B/at): μ_x	−0.58(11)	−1.38(7)	–
μ_y	–	0.92(4)	–
μ_z	0.53(5)	1.42(5)	–
μ_t	0.79(7)	2.18(6)	–
R_B	4.43	3.59	3.52
R_{mag}	7.50	7.55	5.61
R_{wp}	3.61	3.58	3.15
χ^2	1.57	1.54	1.74

theoretical values of 3 μ_B/at. However, the Tm sublattice is not fully polarized at 2 K, reaching a value of 2.18 μ_B/at, well below the free ion Tm^{3+} moment of 7 μ_B. Tm^{3+} moments are ordered following the same Irrep (mGM_2^+). They are coupled antiferromagnetically to the Co-Mn sublattice in the ac plane, but they also have a y component so that the Tm^{3+} moments exhibit a small AFM canting (A type) along the b direction. The magnetic (Shubnikov) space group (see Table III) that gives account of the order described in A and B sublattices is $P2_1'/c'$ (14.79, a nonpolar group). The best refinements at 2 K and the temperature dependence of the magnetic moments using the D1B data are shown in the Supplemental Material [30], and the resulting magnetic structure is displayed in the inset of Fig. 1(b).

Regarding the Ho_2CoMnO_6 sample, similar results were found for the Co/Mn sublattice, but in this case there is no second magnetic transition due to the long-range ordering of Ho^{3+} moments. In this sample, the F phase starts at ∼80 K [see Figs. 1(a) and 1(c)], and the temperature dependence for the intensity of magnetic peaks follows a Langevin-like behavior below T_C (see Supplemental Material [30]). At very low temperature, an anomalous background increase at $2\theta \sim 20^\circ$ reveals the onset of the magnetic contribution from the Ho sublattice, which is of very short range (indicated as Ho-SR in Fig. 1). To avoid this irregular background, the high resolution neutron pattern was collected at 10 K, and the refinement can be seen in the Supplemental Material [30], whereas the refined data is also included in the Table II. The resulting magnetic structure is plotted in the inset of Fig. 1(a), and the magnetic ordering of the Mn/Co sublattice follows the same Irrep as Tm_2CoMnO_6, with an F_xF_z arrangement and $P2_1'/c'$ magnetic symmetry achieving a value of 2.92 μ_B/at.

TABLE III. Magnetic structures representative of the FM and E-type magnetic orders at 2 K for Tm_2CoMnO_6 and Yb_2CoMnO_6 double perovskites, respectively.

	Tm_2CoMnO_6 at 2 K	Yb_2CoMnO_6 at 2 K
Magnetic space group	$P2'_1/c'$ (14.79)	P_a2_1 (4.10)
Transformation to standard setting	$(a, b, a+c; 0, 0, 0)$	$(-c, b, a; 1/4, 0, 1/8)$
Magnetic unit cell	$a = 5.1894(1)$	$a = 5.1780(2)$
	$b = 5.5430(1)$	$b = 5.5472(2)$
	$c = 7.4193(2)$	$c = 14.8154(3)$
	$\beta = 89.674^\circ$	$\beta = 90.378^\circ$
Magnetic point group	$2'/m'$ (5.5.16)	$21'$ (3.2.7)
Refined moments (μ_B):		
Co (1/2, 0, z)	(1.13[9], 0, −2.60[5]) $z = 1/2$	(0.66[5], 0, 1.53[4]) $z = 1/4$
Mn (1/2, 0, 0)	(1.13[9], 0, −2.60[5])	(0.66[5], 0, 1.53[4])
Tm (0.021, 0.073, 0.252)	(−1.38[7], 0.92[4], 1.42[5])	
Yb1 (0.018, 0.074, 0.374)		(0, 0, 0)
Yb2 (0.981, 0.925, 0.625)		(0, 0, 0.65[3])

C. Magnetic ordering in $Yb_{2-x}Lu_xCoMnO_6$ ($x = 0, 1, 2$)

These three samples show similar magnetic behavior of the Mn/Co sublattice. As outlined previously for Yb_2CoMnO_6 [15], the magnetic contribution is small and subtle, but the magnetic peaks clearly follow the propagation vector $\mathbf{k} \sim (0, 0, 1/2)$. Due to the small magnitude of the magnetic peaks, the study of the magnetic structure of these compounds has focused on the D1B data, more sensitive to the magnetic contribution owing to its high neutron flux and low background. Figures 2(a) and 2(b) compare the neutron patterns above and below the magnetic transition and show the difference patterns for Lu_2CoMnO_6 and Yb_2CoMnO_6. In the former sample, the magnetic contribution is focused in three families of peaks: {1 1 ½}, {1 1 3/2}, and {0 2 ½}. This result is in agreement with an E-type AFM structure. In addition, reflections like (0 0 l/2) are very weak, indicating that the spin direction is mainly along the c axis. The Yb_2CoMnO_6 compound shows an additional magnetic contribution arising from the long-range ordering of Yb moments, which develops at a temperature lower than the Mn/Co order. It is characterized by the small (0 1 ½) peaks and a strong diffuse scattering at low angles around the (0 0 ½) peak [see Fig. 2(b)], suggesting short-range ordering. Figure 2(c) shows the temperature dependence of some characteristic magnetic peaks. The Mn/Co order is developed around 50 K, whereas the Yb order is established at about 15 K.

Two additional features are seen in these diffraction patterns [Fig. 2(d)]. First, there exists a systematic shift of the E-type magnetic reflections from their theoretical positions; second, certain reflections, e.g., (0 0 l/2), have a strongly asymmetric peak shape, with relatively broad tails on the high angle side [15]. Both features are commonly observed in systems with stacking faults [31,32]. In the present case, only magnetic reflections show these features, so we guess that these faults affect only the spin arrangement. It is well known that dislocation defects and antiphase boundaries are normally present in double perovskites [18,33,34]. Antiphase boundaries are typically associated with ASDs, such as those present in this family of compounds (∼5% of misplaced atoms in our case). These defects may lead to dislocations in the spin arrangement, resulting in a rise of magnetic disorder and small magnetic domains with a reduced magnetic moment relative to a sample without defects. An earlier study suggested [12] that the Mn/Co ordering is incommensurate in the ab plane for Lu_2CoMnO_6. We have tested this and other possible incommensurate magnetic structures, but the corresponding peak splitting failed to account for the broadening and shift of the magnetic peaks. Therefore, we conclude that the particular shape of these reflections is due to the abovementioned extended defects. Accurate refinements of neutron patterns with these defects are very difficult, and some refined parameters must be taken with care. In our case, we have used the FullProf program to refine these patterns using a phenomenological treatment of some individual magnetic reflections with selective shifts and broadenings. A representative fit of Yb_2CoMnO_6 is shown in the Supplemental Material [30], and the refined data are summarized for the three samples in the Table IV. These refinements suggest that ordered moments are well below the theoretical values for a fully saturated Mn/Co sublattice, indicating that extended defects do not participate in the long-range ordering. Crystallite size analysis with the Scherrer equation on the (1 1 3/2) magnetic reflection has been used to estimate the ordered domain size, i.e., the size of the ordered region between defects, yielding a few tens of nanometers (Table IV). The ordered magnetic moments are mainly located in the ac plane with a main component along the c axis (similar direction to the one observed for the related FM compounds). Figure 2(e) shows the magnetic structure at 2 K for Lu_2CoMnO_6 and Yb_2CoMnO_6 with the E-type magnetic arrangement of the metals in the ac plane. The latter one in addition shows a partial order of the Yb sublattice. The magnetic symmetry in both compounds is P_a2_1 (4.10). In this symmetry, Yb atoms split in two different orbits in the magnetic cell (see Table III for additional details). In one of them (Yb1 orbit), the Yb atoms experience a strong internal field from the FM arrangement of neighboring Mn/Co moments, which prevents the AF coupling between Yb atoms and keeps them disordered. In the other position (Yb2) instead, the AFM arrangement of neighboring Mn/Co moments cancels the internal field at the Yb position and the magnetic Yb-Yb interaction produces a long-range AFM ordering in these atoms below 15 K [see Fig. 2(e)]. Curiously, the ordering

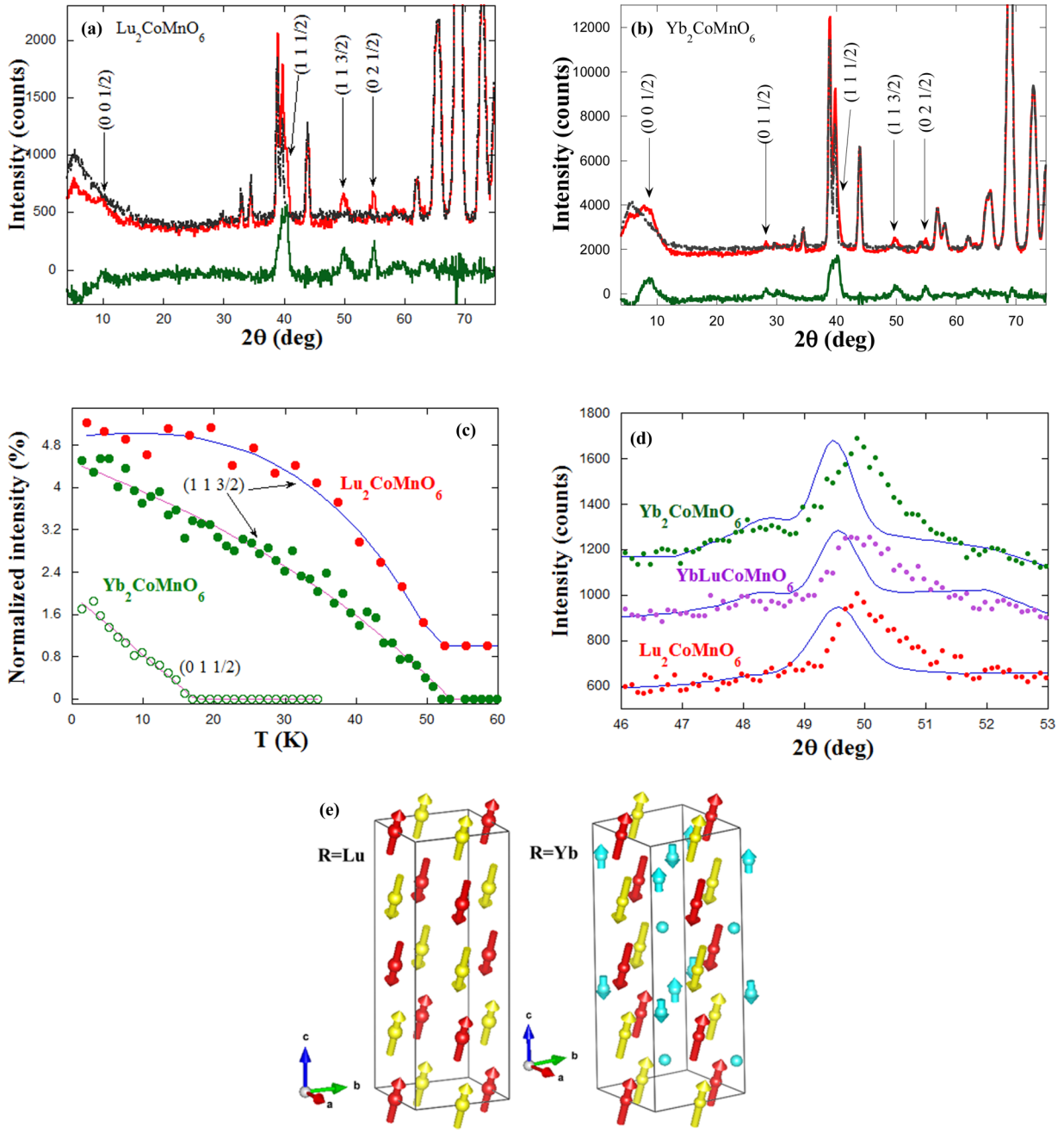

FIG. 2. Comparison of the neutron patterns above (60 K, black line) and below (2 K, red line) of the magnetic transition for (a) $Lu_2CoMnCO_6$ and (b) Yb_2CoMnO_6. The temperature difference pattern is shown at the bottom of each figure. (c) The temperature dependence of selected magnetic peaks—the intensity is normalized respect to the most intense peak in the neutron pattern, i.e., (022)—and the data of Lu_2CoMnO_6 have been shifted upward. (d) Detail of the neutron patterns around the (1 1 3/2) magnetic peak and the theoretical profile obtained with the instrumental resolution. (e) Magnetic structure of Lu_2CoMnO_6 and Yb_2CoMnO_6 deduced from the neutron refinements. Yellow, red, and blue arrows stand for Mn, Co, and Yb moments, respectively.

of this Yb sublattice is still present in $YbLuCoMnO_6$ in spite of the strong dilution with Lu atoms.

D. Metamagnetic transitions

A phase transition induced by an external magnetic field in Yb_2CoMnO_6 has been reported in our previous paper [15]. Now, we report the observation of similar features for all $Yb_{2-x}Lu_xCoMnO_6$ samples exhibiting E-type ordering at zero field. Isothermal measurements of neutron patterns at 2 and 25 K were collected by varying the magnetic field in steps of 5 kOe. The results are shown in Fig. 3. The data at 2 K show a strong change in the neutron patterns for a magnetic field around 25 kOe. Above this threshold field, the intensity of magnetic peaks produced by the E-type ordering decreases, whereas the (1 1 0) and related peaks become more intense. These features agree with a spin reorientation at high fields, giving rise to a collinear FM ordering of Mn/Co moments (F

TABLE IV. Refined structural parameters (lattice, fractional coordinates, temperature factors, and magnetic moments) and reliability factors from neutron patterns collected at low temperature for Yb_2CoMnO_6, $YbLuCoMnO_6$, and Lu_2CoMnO_6. The Wyckoff positions are indicated for each atom in $P2_1/n$ setting.

Sample	Yb_2CoMnO_6	$YbLuCoMnO_6$	Lu_2CoMnO_6
Lattice a (Å)	5.1780(2)	5.1756(3)	5.1624(3)
b (Å)	5.5472(2)	5.5524(3)	5.5475(4)
c (Å)	7.4077(3)	7.4175(4)	7.4074(5)
β (deg)	90.378(4)	90.386(6)	90.411(6)
Volume (Å^3)	212.77(2)	213.15(2)	212.13(2)
Coordinates R (4e): x	0.0210(3)	0.0213(4	0.0206(4)
Y	0.0745(8)	0.0741(3)	0.0744(4)
Z	0.7486(3)	0.7490(4)	0.7496(5)
O1 (4e): x	0.2988(7)	0.2985(7)	0.3006(7)
Y	0.3215(8)	0.3209(8)	0.3203(8)
Z	0.9474(6)	0.9491(6)	0.9462(6)
O2 (4e): x	0.3268(7)	0.3280(7)	0.3256(7)
Y	0.2955(7)	0.2960(7)	0.2964(6)
Z	0.5598(5)	0.5614(5)	0.5600(5)
O3 (4e): x	0.8858(5)	0.8851(5)	0.8830(5)
Y	0.4565(4)	0.4578(5)	0.4559(5)
Z	0.7609(5)	0.7619(5)	0.7589(5)
B_{av} (Å^2)	0.68(5)	0.44(6)	0.38(4)
Mn/Co moment (μ_B/at): μ_x	0.66(5)	0.41(6)	0.47(3)
μ_z	1.53(4)	1.24(3)	1.28(2)
μ_t	1.66(4)	1.31(4)	1.36(2)
Domain size: ξ (Å)	210	160	360
Yb moment (μ_B/at): μ_z	0.65(3)	0.89(12)	–
R_B	1.8	2.5	2.4
R_{mag}	4.4	6.2	4.7
R_{wp}	3.1	3.6	3.8
χ^2	2.2	1.9	1.9

phase) in the ac plane with a main component along the c axis and the same magnetic symmetry ($P2_1'/c'$, 14.79), as reported for Ho_2CoMnO_6 in the inset of Fig. 1(a). As can be seen in the inset of Fig. 3(a), the transformation is not completed at 2 K in our measurements, and remains of E-type phase ($\sim$ 4%) persist at 50 kOe. On the other hand, at 25 K the transformation from E phase into the F one is already observed at 5 kOe, and it is completed at 45 kOe [see Fig. 3(b)]. Therefore, the

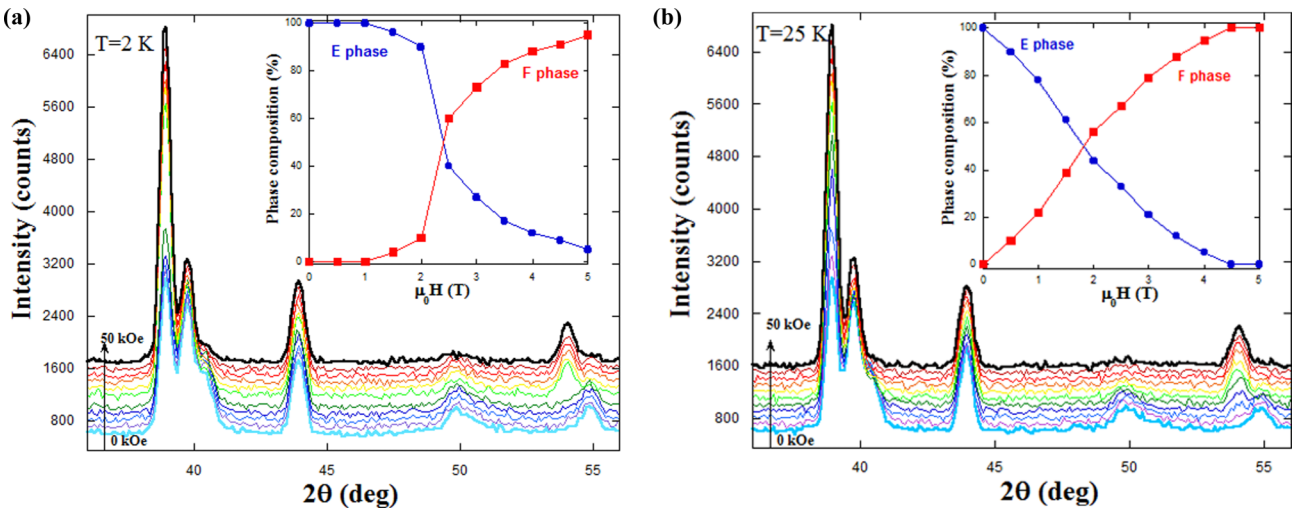

FIG. 3. Detail of the neutron patterns of Lu_2CoMnO_6 under an external magnetic field at (a) 2 K and (b) 25 K. Magnetic field is increased in steps of 5 kOe. Insets: Magnetic dependence of the magnetic phases at the temperature indicated for each plot.

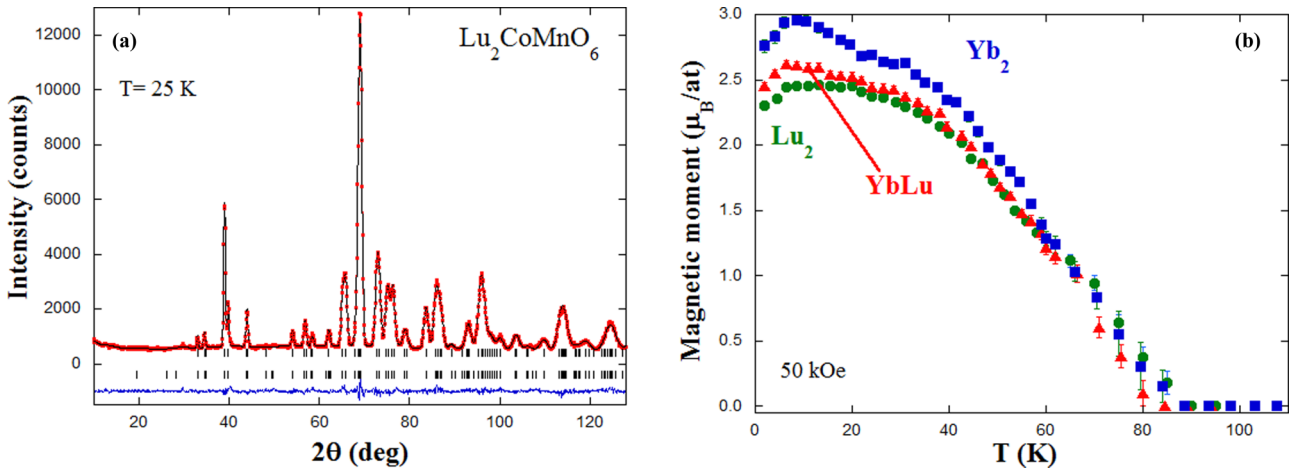

FIG. 4. (a) Rietveld refinement of neutron pattern collected at D1B of Lu_2CoMnO_6 at 25 K and 50 kOe. Red points and the black line stand for experimental and calculated pattern, respectively. The difference is plotted at the bottom (blue line) and allowed reflections (nuclear and magnetic) are also indicated as bars. (b) Temperature dependence of refined magnetic moments of the Co/Mn sublattice for the F phase of $Yb_{2-x}Lu_xCoMnO_6$ (the rare earth ratio is indicated for each curve).

metamagnetic transition is observed at lower magnetic fields as the temperature increases. Similar results were obtained for the other two samples (not shown here).

Figure 4(a) shows the refinement of the Lu_2CoMnO_6 sample at 25 K and at 50 kOe using a collinear FM phase with the refined moments of $m_x = 1.02(5)\,\mu_B$/at and $m_z = 2.15(3)\,\mu_B$/at. In Fig. 4(b), we show the temperature dependence of the refined moments for the Co/Mn sublattice from the neutron patterns, which were collected under a magnetic field of 50 kOe. The three samples show the same trend. At low temperature, the size of the ordered moments first increases as the temperature increases. This is ascribed to the conversion of the remaining E phase (and disordered boundaries) into the F phase, which overcomes the usual temperature effect on the moment alignments. At higher temperature, the moments follow the usual monotonic decrease with the temperature up to ~80 K, where the samples become paramagnetic. Comparing with the results at zero field, we observe that the magnetic transition temperature moves up by about 30 K at 50 kOe. Regarding the absolute value of the refined moments, the Yb-based sample shows the highest values, very close to the expected ones for a fully saturated Mn/Co sublattice, whereas the Lu-based sample shows the lowest values in the series. This may be attributed to the stability of the E phase in compounds with smaller rare earth size. Consequently, the features of the E-type phase persist in the neutron patterns up to about 13 K in the Yb-based sample, but they remain up to 24 K for the Lu one.

E. Magnetic properties

Figure 5 shows the temperature scans of dc magnetization for the five samples studied. The measurements were taken in a magnetic field of 100 Oe after zero field cooling (ZFC) and field cooling (FC) in the same field. Clear magnetic transitions are observed for all samples, in agreement with the onset of magnetic contribution in the neutron patterns. The magnetic transition temperature decreases with decreasing the size of rare earth atoms. This is correlated to the increase of the structural distortion that weakens the superexchange interactions between Mn and Co atoms. As in related materials [18,19,27,29], the dc magnetization curves display strong irreversibility between ZFC and FC conditions. The ZFC branches show broad peaks, while the FC ones exhibit a FM-like transition. These features are tentatively ascribed to the dynamics of magnetic domain walls for Ho- and Tm-based compounds since the long-range F ordering was clearly observed in their neutron patterns. For the other three samples, a large amount of extended defects does not allow excluding the presence of a glassy phase.

Figure 6(a) shows the temperature dependence of the real part of the ac susceptibility (χ'_{ac}) at different frequencies for two characteristic samples: Ho_2CoMnO_6 with an F ordering and Lu_2CoMnO_6 with an E-type arrangement. In both cases, the magnetic transition is characterized by a sharp peak. Though the peak does not shift with the frequency of the magnetic field, both samples show quite different dynamic behavior

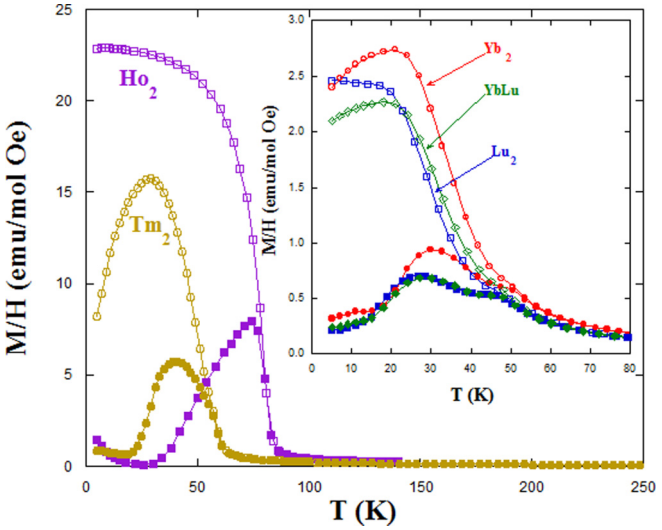

FIG. 5. The dc magnetization versus temperature in ZFC (dark symbols) and FC (open symbols) conditions for Ho_2CoMnO_6 (circles), Tm_2CoMnO_6 (squares), and (inset) $Yb_{2-x}Lu_xCoMnO_6$.

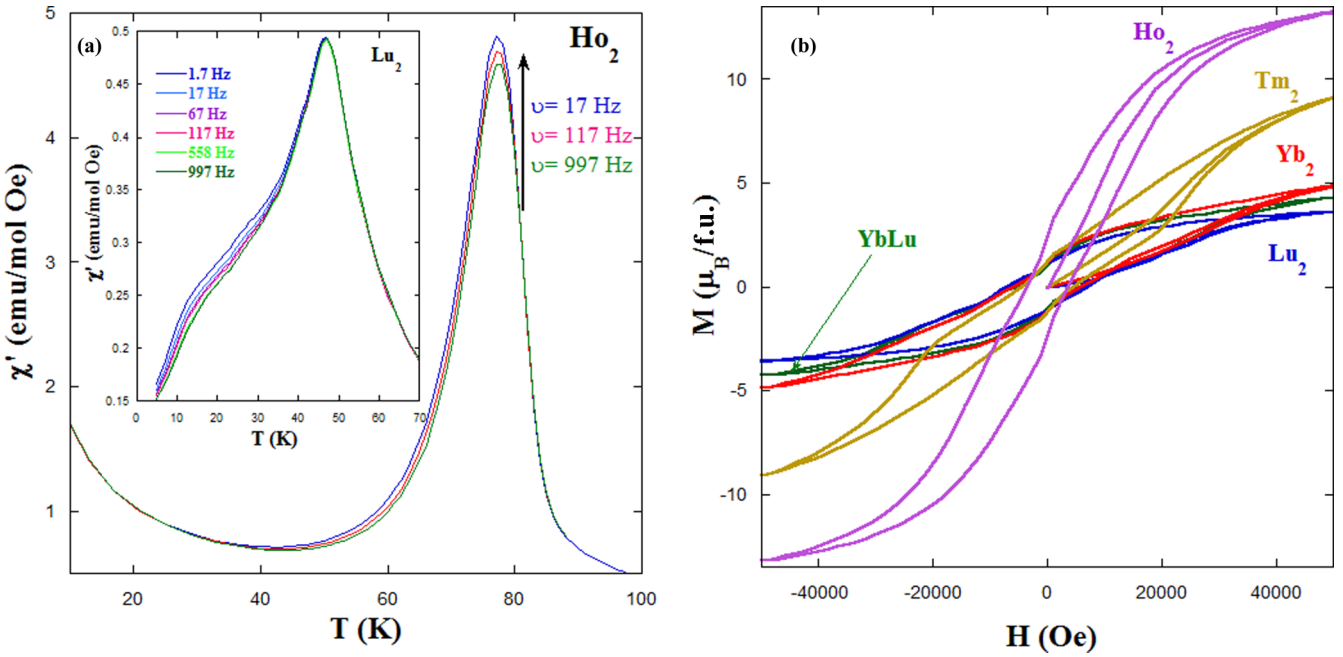

FIG. 6. (a) Temperature dependence of the in phase component of ac magnetic susceptibility for a series of frequencies between 17 and 997 Hz for Ho_2CoMnO_6 (main panel) and Lu_2CoMnO_6 (inset). (b) Hysteresis loops for all samples at 5 K.

in the χ'_{ac} curves. In the Ho-based sample, the main dynamic behavior is concentrated at the peak intensity, which decreases as the frequency increases. At temperatures below T_C, the dynamic behavior diminishes and vanishes at ∼50 K. Similar effects were observed in Y_2CoMnO_6 and may be ascribed to magnetic disaccommodation effects of pinned domain walls, as in related perovskites [18]. As previously observed [12,35], the frequency dependence of χ'_{ac} is less pronounced at the peak of Lu_2CoMnO_6, while the dynamic behavior is significant at lower temperatures (∼ 20 K) where the χ'_{ac} curve exhibits a broad shoulder. This feature is also observed in the other $Yb_{2-x}Lu_xCoMnO_6$ samples [15], and it might be related to the dynamic behavior of the regions with extended defects (not contributing to the long-range E ordering).

Above the magnetic transition, the temperature dependence of the inverse magnetic susceptibility is linear for all samples up to room temperature, which follows the Curie-Weiss law (not shown here). We have summarized the results from the fits to this law in Table V. In all cases, the Weiss constant (θ) is positive in agreement with the presence of dominant FM interactions. Initially, θ decreases as the rare earth size diminishes (weak FM interaction), reaches its minimum value for R = Yb, but, surprisingly, it increases for $YbLuCoMnO_6$ and Lu_2CoMnO_6 although these compounds do not show any F order at low magnetic fields. The effective magnetic moments (ρ_{eff}) obtained from these fits nicely agree with the expected ones [36] from magnetic contributions of Mn^{4+} (spin only, 3.8 μ_B), Co^{2+} (experimental value, 4.8 μ_B), and R^{3+} (J value).

A spontaneous magnetization is clearly seen in the hysteresis loops measured at 5 K [see Fig. 6(b)]. Saturation is not achieved for H = 50 kOe in any of these samples. In the case of Ho- and Tm-based samples, the magnetization at 50 kOe exceeds the expected value for a fully saturated Co/Mn sublattice (6 μ_B/f.u.), suggesting that the R sublattice also participates in the F order at high fields. This implies the Ho polarization in the first case and the spin reorientation of Tm^{3+} moments in the second sample. In this way, the inflection point at 20 kOe in its $M(H)$ loop may mark the onset of the spin reorientation of Tm. In the case of the samples with E-type ordering ($Yb_{1-x}Lu_xCoMnO_6$ samples), the loops do not reach saturation at 50 kOe, and the corresponding magnetization is well below the theoretical one for the FM coupling of Mn^{4+} and Co^{2+} moments, as inferred from neutron diffraction at high fields. In addition, the samples show high coercive fields and high remanences, typical of hard magnets. These features

TABLE V. Curie constant, Weiss parameter, experimental, and theoretical effective paramagnetic moments obtained from the linear fits of the inverse of susceptibility above the magnetic transition.

Sample	C (emu K^{-1}mol^{-1})	θ (K)	ρ_{eff} (μ_B/f.u.)	ρ_{theo} (μ_B/f.u.)
Ho_2CoMnO_6	32.1	17.7	16.0	16.2
Tm_2CoMnO_6	19.45	15	12.5	12.3
Yb_2CoMnO_6	10.0	12.6	8.95	8.9
$YbLuCoMnO_6$	6.5	33.5	7.2	7.6
Lu_2CoMnO_6	5.15	44.2	6.4	6.2

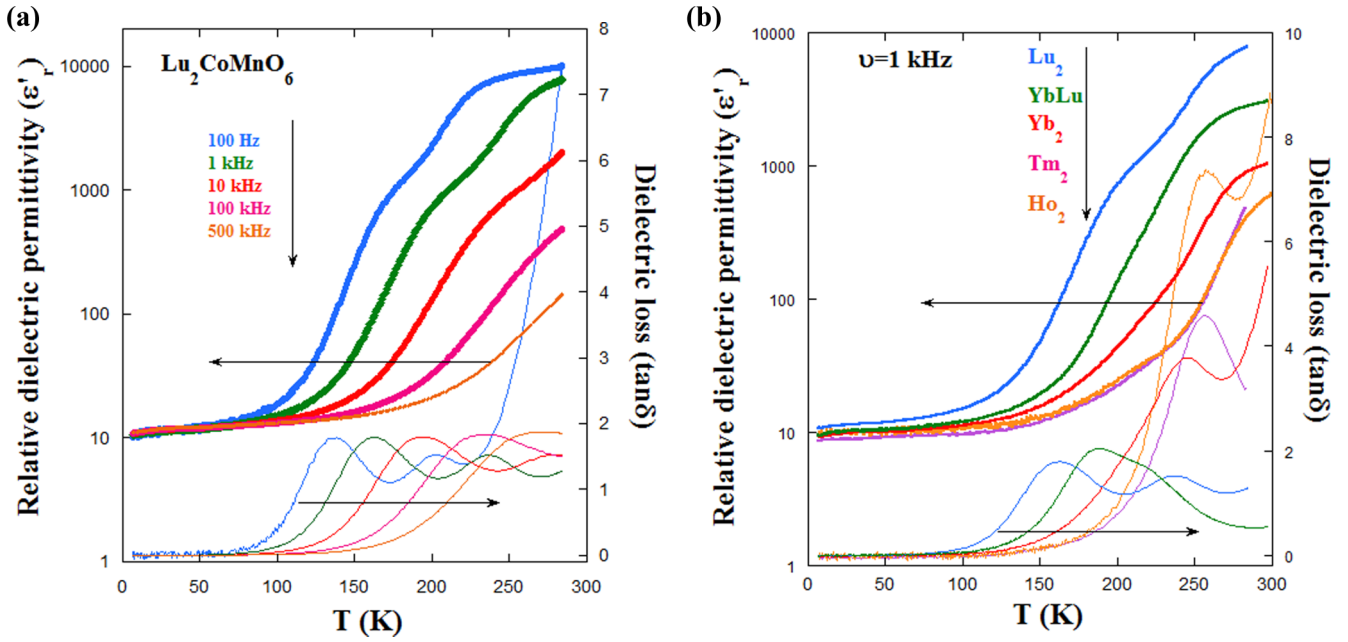

FIG. 7. (a) Temperature dependence of the dielectric constant (ε'_r) and the dielectric loss (tan δ) at five selected frequencies for Lu_2CoMnO_6. (b) Temperature dependence of ε'_r and tan δ of all samples at a frequency of 1 kHz.

might be ascribed to the presence of defects that pin magnetic domains.

F. Electrical properties

All of these samples show semiconducting behavior as the electrical resistivity increases with decreasing temperature. Previous studies on the complex dielectric permittivity of related double perovskites have shown large values of the real part (ε'_r or dielectric constant) at room temperature [18,19,27,29] with a strong decrease down to values of ∼10–26 upon cooling below 50 K. The low temperature values are frequency independent in contrast to the high temperature values that show a strong dynamic behavior. We have observed similar properties in present samples. For instance, Fig. 7(a) displays the temperature dependence of the dielectric constant and the dielectric loss factor (tan δ) for Lu_2CoMnO_6 at five selected frequencies. Similar results were obtained for the rest of the samples. The temperature dependence of ε'_r unveils a steplike increase from a low-temperature value of ∼10 to values of $\sim 10^3$ at room temperature. The step shifts to higher temperatures with increasing frequency, and it is accompanied by a peak in the tan δ. Above this peak, tan δ rises in the low frequency measurement, indicating a strong

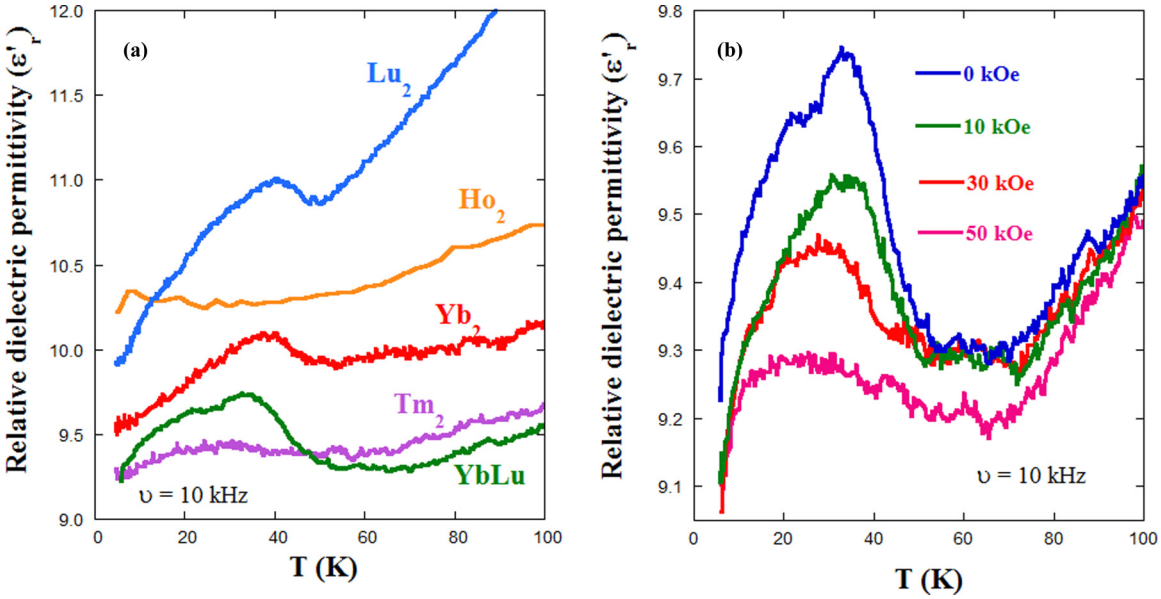

FIG. 8. (a) Temperature dependence below 100 K of the real part of relative dielectric permittivity (ε'_r) for all samples at 10 kHz. (b) Temperature dependence of ε'_r for $YbLuCoMnO_6$ under different magnetic fields.

electronic contribution at room temperature. These effects are usually ascribed to the occurrence of Maxwell-Wagner contributions coming from depletion layers at the interface of grain boundaries or at electrodes [37–39], and they were also reported in related double perovskites [18,19]. Figure 7(b) compares the $\varepsilon'_r(T)$ and $\tan\delta(T)$ curves of all samples measured at 1 kHz. R_2CoMnO_6 (R = Ho, Tm, Yb) samples show similar curves with the steplike increase in the $\varepsilon'_r(T)$ curve and the peak in the $\tan\delta(T)$. These features are shifted to lower temperature as the rare earth size diminishes. Moreover, two steps are clearly identified in the Lu-based samples. However, the most significant differences among these samples are present at low temperature. Figure 8(a) shows, in detail, the temperature dependence of ε'_r below 100 K. The samples with an E-type magnetic order show an anomaly in the $\varepsilon'_r(T)$ curves whose onset coincides with the magnetic transition temperature. However, the samples with an F order do not show any anomaly in the dielectric constant at low temperatures. These results are in agreement with previous reports on Lu_2CoMnO_6 and Yb_2CoMnO_6 samples [12,15,40]. The presence of a magnetic field strongly affects the size of the anomaly in samples with E phase. It decreases as the magnetic field increases and almost disappears at 50 kOe, as can be seen for $YbLuCoMnO_6$ in Fig. 8(b). This is related to the metamagnetic transition shown in Fig. 3 and leads to the negative magnetocapacitance observed in these samples [12,15,40].

Another striking point in the electrical properties of these compounds is the presence of ferroelectric ordering. As shown in Table III for the samples presenting E-type magnetic ordering, the associated magnetic space group P_a2_1 (4.10) is not centrosymmetric and polar. The point symmetry 21' (3.2.7) prohibits any FM component, but it allows the formation of electrical dipoles parallel to the b axis in the monoclinic $P2_1/n$ cell (P_y). The inversion center is broken here due to the combination of the modulations coming from B-site ordering and the E-type magnetic ordering [14]. In a previous study on Yb_2CoMnO_6, we emphasized that the measurement of the pyroelectric effect failed to detect any significant electric polarization at the magnetic transition [15], in agreement with studies performed on Lu_2CoMnO_6 single crystals [13]. Our aim in preceding measurements was the detection of ferroelectricity associated with the magnetic transition so that the poling field was established at 70–80 K and no remarkable pyroelectric current was detected [15]. Later on, pyroelectric currents have been detected in a high number of double perovskites [16,41], but we determined that they are due to extrinsic effects for Y- and Er-based compounds [18,19]. Here, we have repeated some of these measurements in $Yb_{2-x}Lu_xCoMnO_6$ samples but performing the electric poling at 150 K. In these conditions, a reversible pyroelectric current is observed, as can be seen in Fig. 9(a) for the case of the Yb-based sample. The temperature dependence of the calculated polarization (P) resembles a ferroelectric transition, but the Curie temperature is well above the magnetic transition temperature, suggesting different origins for the two properties. In fact, the peak of depolarization current [see the inset of Fig. 9(a)] is strongly dependent on the heating rate, indicating that this current arises from either depolarization of trapped charges or defect dipole reorientation [18,42–45].

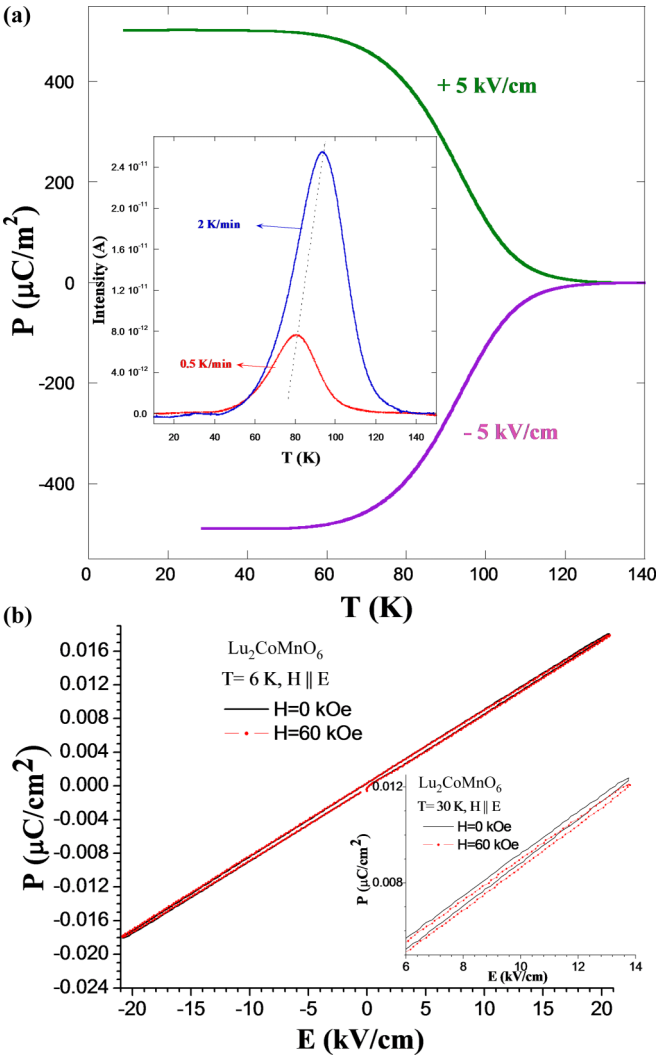

FIG. 9. (a) Temperature dependence of polarization for Yb_2CoMnO_6 sample obtained by integrating the pyroelectric currents. (Inset) Temperature dependences of pyroelectric currents for Yb_2CoMnO_6 obtained with the same poling field of 5 kV/cm and different heating rates. (b) $P(E)$ curves measured on the Lu_2CoMnO_6 with $H = 0$ and 60 kOe with the electric field along magnetic field direction at 6 K for a frequency of 100 Hz. Inset: Detail of the same measurements at 30 K.

Electric-field-dependent polarization [$P(E)$] measurements were carried out at low temperature for $Yb_{2-x}Lu_xCoMnO_6$ samples to check for the existence of a ferroelectric loop. We show in Fig. 9(b) the results obtained for Lu_2CoMnO_6 (similar results were observed in the rest of the samples). It is noteworthy that the $P(E)$ dependence at 6 K is a straight line, and no differences are observed under a magnetic field of 60 kOe. When these measurements are repeated at 30 K, i.e., close to the maximum of the anomaly observed in the $\varepsilon'_r(T)$ curve, the same linear behavior is observed, but a small decrease in the $P(E)$ slope is noticeable after applying the magnetic field. This feature agrees with a negative magnetocapacitance of about 3%, a similar order of magnitude than the one inferred from the curves of Fig. 8(b). The linear dependence of the $P(E)$ loops confirms the lack of

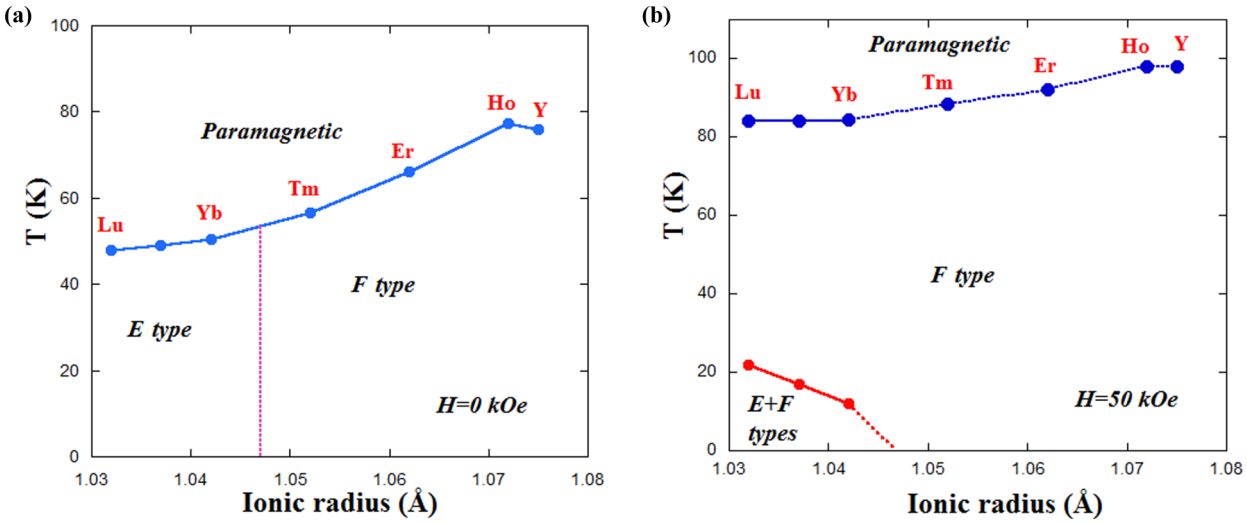

FIG. 10. (a) Phase diagram for R_2CoMnO_6 samples without magnetic field. (b) The same phase diagram under a magnetic field of 50 kOe. Data for $R = Y$ and Er have been taken from Refs. [18] and [19]. Ionic radiuses are taken from Ref. [46] for R^{3+} cations in ninefold coordination. Continuous lines indicate values obtained from neutron diffraction data, whereas the dotted line designed values inferred from magnetic measurements or extrapolations.

spontaneous polarization in these compounds. This result is at odds with earlier theoretical predictions [9,11] or symmetry analysis [14]. The latter suggests that polarization comes from the symmetry break of the oxygen atoms yielding a polarization parallel to the b axis, in agreement with the anisotropy observed in the anomaly of $\varepsilon'_r(T)$ curves measured in single crystals [13]. A possible explanation to account for this discrepancy may be based on the magnetic ordering in these samples. Theoretical studies are made on ideal samples with a perfect arrangement of atoms and spins. Our study has revealed the presence of extended defects in the E phase of these perovskites, resulting in magnetic domains of a few tens of nanometers. This large amount of defects may lead to small ferroelectric domains, hard to detect, or even prevent the formation of long-range dipole ordering.

IV. CONCLUDING REMARKS

We here report a thorough paper on the magnetoelectric properties of R_2CoMnO_6 perovskites with heavy R atoms and a high degree of Co^{2+}/Mn^{4+} ordering ($\sim 95\%$). Two competitive magnetic phases exist in the R_2CoMnO_6 phase diagram (see Fig. 10), and its prevalence depends on the rare earth ionic radius (r_R^{3+}) and the external magnetic field. In the absence of magnetic field, the F phase is observed down to $r_{Tm}^{3+} = 1.052$ Å, whereas below $r_{Yb}^{3+} = 1.042$ Å [46], the E phase becomes more stable. This fact is related to the enhancement of NNN AFM interactions in perovskites with a strong structural distortion (due to the small r_R^{3+}), which competes with NN FM interactions. The critical radius should be between r_{Tm}^{3+} and r_{Yb}^{3+}, positioned in the midpoint of Fig. 10(a) as a first approximation. However, the E phase is not fully established as neutron patterns reveal broad and shifted magnetic peaks, indicating the occurrence of a large amount of extended defects, predictably stacking faults. The application of a magnetic field destabilizes the E phase and induces its transformation into the F phase so that the E phase has practically vanished at 50 kOe [see Fig. 10(b)]. This metamagnetic transition—P_a2_1 (4.10) $\rightarrow$ $P2'_1/c'$ (14.79)—leads to a negative magnetocapacitive effect. Indeed, $Yb_{2-x}Lu_xCoMnO_6$ shows an anomaly in the dielectric constant coupled to the onset of long-range magnetic ordering. This was ascribed to the break of the inversion center induced by the onset of E-type magnetic ordering, and ferroelectric ordering was expected [11,14,17]. We did not detect any evidence of spontaneous electric polarization in our samples. Instead we found thermally stimulated depolarization currents ascribed to defects in the samples. The lack of observable ferroelectricity might be due to the presence of the above-mentioned extended defects and the consequent small size of magnetic domains in the E phase.

ACKNOWLEDGMENTS

We acknowledge ILL and D1B-CRG Ministerio de Economía y Competitividad (MINECO) for beam time allocation (experiment codes CRG-2419, CRG-2154, and 5-31-2233) and the use of Servicio General de Apoyo a la Investigación (SAI), Universidad de Zaragoza. We are thankful for financial support from Spanish MINECO Projects No. MAT2015-68760-C2-1 and No. MAT2015-68760-C2-2, cofunded by European Regional Development Fund (ERDF) from the European Union, the Severo Ochoa Programme (Grant No. SEV-2015-0946), and DGA (Grant No. E69-CAMRADS).

[1] M. Fiebig, J. Phys. D: Appl. Phys. **38**, R123 (2011).
[2] M. Fiebig, T. Lottermoser, D. Meier, and M. Trassin, Nat. Rev. Mater. **1**, 16046 (2016).
[3] J. Blasco, S. Lafuerza, J. García, G. Subías, V. Cuartero, J. L. García-Muñoz, C. Popescu, and I. Peral, Phys. Rev. B **93**, 184110 (2016).

[4] C. Becher, L. Maurel, U. Aschauer, M. Lilienblum, C. Magén, D. Meier, E. Langenberg, M. Trassin, J. Blasco, I. P. Krug, P. A. Algarabel, N. A. Spaldin, J. A. Pardo, and M. Fiebig, Nat. Nanotechnol. **10**, 661 (2015).

[5] S.-W. Cheong and M. Mostovoy, Nat. Mater. **6**, 13 (2007).

[6] T. Kimura, Annu. Rev. Condens. Matter Phys. **3**, 93 (2012).

[7] V. Cuartero, S. Lafuerza, G. Subías, J. García, E. Schierle, J. Blasco, and J. Herrero-Albillos, Phys. Rev. B **91**, 165111 (2015).

[8] T. Kimura, S. Ishihara, H. Shintani, T. Arima, K. T. Takahashi, K. Ishizaka, and Y. Tokura, Phys. Rev. B **68**, 060403(R) (2003).

[9] I. A. Sergienko, C. Sen, and E. Dagotto, Phys. Rev. Lett. **97**, 227204 (2006).

[10] T. Goto, T. Kimura, G. Lawes, A. P. Ramirez, and Y. Tokura, Phys. Rev. Lett. **92**, 257201 (2004).

[11] S. Kumar, G. Giovannetti, J. van den Brink, and S. Picozzi, Phys. Rev. B **82**, 134429 (2010).

[12] S. Yañez-Vilar, E. D. Mun, V. S. Zapf, B. G. Ueland, J. S. Gardner, J. D. Thompson, J. Singleton, M. Sánchez-Andujar, J. Mira, N. Biskup, M. A. Señaris-Rodríguez, and C. D. Batista, Phys. Rev. B **84**, 134427 (2011).

[13] N. Lee, H. Y. Choi, Y. J. Jo, M. S. Seo, S. Y. Park, and Y. J. Choi, Appl. Phys. Lett. **104**, 112907 (2014).

[14] J. M. Perez-Mato, S. V. Gallego, L. Elcoro, E. Tasci, and M. I. Aroyo, J. Phys.: Condens. Matter **28**, 286001 (2016).

[15] J. Blasco, J. L. García-Muñoz, J. García, J. Stankiewicz, G. Subías, C. Ritter, and J. A. Rodríguez-Velamazán, Appl. Phys. Lett. **107**, 012902 (2015).

[16] G. Sharma, J. Saha, S. D. Kaushik, V. Siruguri, and S. Patnaik, Appl. Phys. Lett. **103**, 012903 (2013).

[17] C. Y. Ma, S. Dong, P. X. Zhou, Z. Z. Du, M. F. Liu, H. M. Liu, Z. B. Yan, and J.-M. Liu, Phys. Chem. Chem. Phys. **17**, 20961 (2015).

[18] J. Blasco, J. García, G. Subías, J. Stankiewicz, J. A. Rodríguez-Velamazán, C. Ritter, J. L. García-Muñoz, and F. Fauth, Phys. Rev. B **93**, 214401 (2016).

[19] J. Blasco, G. Subías, J. García, J. Stankiewicz, J. A. Rodríguez-Velamazán, C. Ritter, and J. L. García-Muñoz, Solid State Phenomena **257**, 95 (2017).

[20] R. I. Dass and J. B. Goodenough, Phys. Rev. B **67**, 014401 (2003).

[21] T. Kyômen, R. Yamazaki, and M. Itoh, Chem. Mater. **15**, 4798 (2004).

[22] J. Rodriguez-Carvajal, Phys. B **192**, 55 (1993).

[23] J. M. I. Aroyo, J. M. Perez-Mato, C. Capillas, E. Kroumova, S. Ivantchev, G. Madariaga, A. Kirov, and H. Wondratschek. Z. Krist. **221**, 15 (2006).

[24] M. I. Aroyo, A. Kirov, C. Capillas, J. M. Perez-Mato, and H. Wondratschek. Acta Cryst. A **62**, 115 (2006).

[25] J. M. Perez-Mato, S. V. Gallego, E. S. Tasci, L. Elcoro, G. de la Flor, and M. I. Aroyo. Annu. Rev. Mater. Res. **45**, 217 (2015).

[26] V. Cuartero, S. Lafuerza, M. Rovezzi, J. García, J. Blasco, G. Subías, and E. Jiménez, Phys. Rev. B **94**, 155117 (2016).

[27] J. Blasco, J. García, G. Subías, J. Stankiewicz, S. Lafuerza, J. A. Rodríguez-Velamazán, C. Ritter, and J. L. García-Muñoz, J. Phys.: Condens. Matter **26**, 386001 (2014).

[28] E. F. Bertaut, Acta Crystallogr. Sect. A **24**, 217 (1968).

[29] A. J. Barón-González, C. Frontera, J. L. García-Muñoz, B. Rivas-Murias, and J. Blasco, J. Phys.: Condens. Matter **23**, 496003 (2011).

[30] See Supplemental Material at http://link.aps.org/supplemental/10.1103/PhysRevB.96.024409 for representative fits of several neutron diffraction patterns.

[31] M. V. Lobanov, M. Greenblatt, E. Caspi, J. D. Jorgensen, D. V. Sheptyakov, B. H. Toby, C. E Botez, and P. W. Stephens, J. Phys.: Condens. Matter **16**, 5339 (2004).

[32] J. Blasco, M. Castro, and J. García, J. Phys.: Condens. Matter **6**, 5875 (1994).

[33] R. Egoavil, S. Hühn, M. Jungbauer, N. Gauquelin, A. Béché, G. Van Tendeloo, J. Verbeeck, and V. Moshnyaga, Nanoscale **7**, 9835 (2015).

[34] T. Asaka, X. Z. Yu, Y. Tomioka, Y. Kaneko, T. Nagai, K. Kimoto, K. Ishizuka, Y. Tokura, and Y. Matsui, Phys. Rev. B **75**, 184440 (2007).

[35] V. S. Zapf, B. G. Ueland, M. Laver, M. Lonsky, M. Pohlit, J. Müller, T. Lancaster, J. S. Möller, S. J. Blundell, J. Singleton, J. Mira, S. Yañez-Vilar, and M. A. Señarís-Rodríguez, Phys. Rev. B **93**, 134431 (2016).

[36] J. M. D. Coey, *Magnetism and Magnetic Materials* (Cambridge University Press, Cambridge, 2010), p. 115.

[37] P. Lunkenheimer, V. Bobnar, A. V. Pronin, A. I. Ritus, A. A. Volkov, and A. Loidl, Phys. Rev. B **66**, 052105 (2002).

[38] P. Lunkenheimer, R. Fichtl, S. G. Ebbinghaus, and A. Loidl, Phys. Rev. B **70**, 172102 (2004).

[39] S. Lafuerza, J. García, G. Subías, J. Blasco, K. Conder, and E. Pomjakushina, Phys. Rev. B **88**, 085130 (2013).

[40] S. Chikara, J. Singleton, J. Bowlan, D. A. Yarotski, N. Lee, H. Y. Choi, Y. J. Choi, and V. S. Zapf, Phys. Rev. B **93**, 180405(R) (2016).

[41] L-Wang, W. Zhou, D. Wang, Q. Cao, Q. Xu, and Y. Du, J. Appl. Phys. **117**, 17D914 (2015).

[42] X. Zhang, Y. G. Zhao, Y. F. Ci, L. D. Ye, D. Y. Zhao, P. S. Li, J.W.Wang, M. H. Zhu, H. Y. Zhang, and G. H. Rao, Appl. Phys. Lett. **104**, 062903 (2014).

[43] N. Horiuchi, Y. Tsuchiya, K. Nozaki, M. Nakamura, A. Nagai, and K. Yamashita, Sol. State Ion. **262**, 500 (2014).

[44] T. Zou, Z. Dun, H. Cao, M. Zhu, D. Coulter, H. Zhou, and X. Ke, Appl. Phys. Lett. **105**, 052906 (2014).

[45] N. Horiuchi, M. Nakamura, A. Nagai, K. Katayama, and Y. Yamashita, J. Appl. Phys. **112**, 074901 (2012).

[46] R. D. Shannon, Acta Cryst. **A32**, 751 (1976).